catalysts

MDPI

Article

Full-Spectrum Photocatalytic Activity of $ZnO/CuO/ZnFe_2O_4$ Nanocomposite as a PhotoFenton-Like Catalyst

Zhenzhen Li, Huabin Chen and Wenxia Liu *

State Key Laboratory of Biobased Material and Green Papermaking, Qilu University of Technology, Shandong academy of sciences, Jinan 250353, China; zhenzhenliqlu@163.com (Z.L.); chenhuabin258259@163.com (H.C.)

* Correspondence: liuwenxia@qlu.edu.cn; Tel.: +86-158-2000-9096

Received: 2 October 2018; Accepted: 16 November 2018; Published: 18 November 2018

Abstract: Deriving photocatalysts by the calcination of hydrotalcite-like compounds has attracted growing interest for extending their photocatalytic activity to the visible and even near-infrared (NIR) light regions. Herein, we describe the acquisition of a $ZnO/CuO/ZnFe_2O_4$ nanocomposite with good photoFenton-like catalytic activity under UV, visible and near-infrared (NIR) light irradiation by optimizing the calcination temperature of the coprecipitation product of Zn^{2+}, Cu^{2+} and Fe^{3+}. The $ZnO/CuO/ZnFe_2O_4$ nanocomposite is composed of symbiotic crystals of ZnO, CuO and $ZnFe_2O_4$, which enable the nanocomposite to show absorption in the UV, visible and NIR light regions and to produce a transient photocurrent in the presence of H_2O_2 under NIR irradiation. The full-spectrum photoFenton-like catalyst shows improved performance for the degradation of methyl orange with an increasing amount of H_2O_2 and is very stable in the recycling process. We believe that the $ZnO/CuO/ZnFe_2O_4$ nanocomposite is a promising full-spectrum photoFenton-like catalyst for the degradation of organic pollutants.

Keywords: Full-spectrum; photocatalysis; photoFenton-like catalyst; $ZnO/CuO/ZnFe_2O_4$ nanocomposite; photodegradation; near-infrared light

1. Introduction

Hydrotalcite-like compounds (HLCs), or layered double hydroxides (LDHs), are a class of anionic clays with brucite-like sheets consisting of adjustable mixed metal hydroxides and interlayer anions [1,2]. Many divalent cations, such as Mg^{2+}, Zn^{2+}, Co^{2+}, Ni^{2+}, Mn^{2+}, Fe^{2+} and Cu^{2+}, and trivalent cations, such as Al^{3+}, Fe^{3+}, Cr^{3+}, Mn^{3+}, Ga^{3+} and In^{3+}, have been reported to be involved in the preparation of HLCs [1–5]. By calcinating the HLCs at high temperatures, mixed metal oxides (MMOs) with heterojunctions at metal oxide interfaces are formed due to dehydration, dehydroxylation and anion decomposition [6]. When photoactive metal oxides with suitable band gap structures are involved, MMOs derived from HLC calcination generally show superior photocatalytic performance compared to single metal oxides as semiconductor photocatalysts due to the extended absorption spectrum of the MMOs and reduced recombination rates for photogenerated carriers [7–9]. Deriving HLC-based photocatalysts by calcination has, therefore, attracted growing interest recently from the viewpoint of designing photocatalysts to either improve their photocatalytic performance [10–13] or extend their photocatalytic activity to the visible light region [14–16].

It is well-known that near-infrared (NIR) light accounts for 44% of the harvestable solar energy. Developing full-spectrum photocatalysts active in the NIR region is necessary for the better use of solar energy in photocatalytic processes [17–22]. Many strategies have been developed for fabricating NIR-active photocatalysts involving combination with upconversion materials [23], sensitization with

NIR-responsive dyes [24], manipulation of defect bands, vacancies, and other photosensitive sites in semiconductors [17,25,26], and the incorporation of narrow-band-gap semiconductors [26]. However, HLC-based photocatalysts with near-infrared (NIR) activity have rarely been reported [27–29]. Of the few reported NIR light active photocatalysts derived from HLC calcination, Er^{3+}-doped $ZnO/ZnAl_2O_4$ multiphase oxide (MPO) was prepared by the calcination of Zn/Al/Er-HLC and acquired its the NIR light activity from the doping of Er^{3+} as an upconversion species in $ZnO/ZnAl_2O_4$ MPO [27]. Er^{3+}-doped ZnO-CuO-$ZnAl_2O_4$-MPO was produced through calcination of Zn/Cu/Al/Er-HLC. It absorbs NIR light because of the incorporation of narrow-band-gap CuO and the doping of Er^{3+}. The excellent NIR photocatalytic performance of Er^{3+}-doped ZnO-CuO-$ZnAl_2O_4$-MPO was ascribed to the formation of n–p–n heterojunctions among Er^{3+}-doped n-$ZnAl_2O_4$, Er^{3+}-doped p-CuO and Er^{3+}-doped n-ZnO, which greatly suppresses the recombination of photogenerated electron–hole pairs and extends the life-times of the charge carriers [28]. The $ZnO/ZnFe_2O_4$ nanocomposite derived from the calcination of Zn/Fe-LDH also absorbs NIR light due to the presence of $ZnFe_2O_4$. However, the separation of photogenerated electron–hole pairs under NIR light irradiation depends on the presence of H_2O_2. Consequently, the $ZnO/ZnFe_2O_4$ nanocomposite catalyzes the degradation of organic pollutants under NIR light irradiation as a photoFenton-like catalyst [29].

Coprecipitation is one of the most popular methods for preparing HLCs [1]. In this work, a new full-spectrum photoFenton-like catalyst $ZnO/CuO/ZnFe_2O_4$ nanocomposite was developed by calcinating the coprecipitation product of Zn^{2+}, Cu^{2+} and Fe^{3+}. The obtained $ZnO/CuO/ZnFe_2O_4$ nanocomposite was found to show good optical absorption from the UV to NIR light regions due to the coexistence of CuO and $ZnFe_2O_4$ and found to possess excellent photocatalytic activities in the presence of H_2O_2 under UV, visible and NIR light. The $ZnO/CuO/ZnFe_2O_4$ nanocomposite has also very stable catalytic activities under all tested light irradiation. This work provides a new idea for developing full-spectrum photoFenton-like catalysts.

2. Results and Discussion

2.1. Preparation and Optimization

The $ZnO/CuO/ZnFe_2O_4$ nanocomposite was prepared by coprecipitation of $Zn(NO_3)_2$, $Cu(NO_3)_2$ and $Fe(NO_3)_3$ with mixed NaOH and Na_2CO_3 followed by calcination of the coprecipitation product. The molar ratios of Zn^{2+} to Cu^{2+} and (Zn^{2+} + Cu^{2+}) to Fe^{3+} were both controlled to be 3:1, enabling the incorporation of suitable amounts of copper oxide and ferrite after calcination. Meanwhile, the formation of oxide and spinel (ferrite) phases depends on the calcination temperature, which consequently affects the photoFenton catalytic activity of the as-prepared catalyst. The crystal phases for the calcination products derived from various temperatures were first analyzed using the X-ray diffraction (XRD) technique. The photoFenton-like catalytic activity was analyzed by comparing the removal rate of methyl orange (MO) in the presence of H_2O_2 under light irradiation with that due to adsorption in the dark without H_2O_2.

Figure 1 shows the XRD patterns and photoFenton-like catalytic activities for the calcination products. As shown in Figure 1, the XRD pattern of the calcination product derived from 200 °C shows only a very weak distinguishable peak assigned to the (003) plane of an HLC, indicating that no oxide phase is formed at 200 °C. However, this calcination product removes a significant fraction of MO in the dark, with a MO removal rate under either UV, visible or NIR light irradiation higher than that in the dark, indicative of good absorption of MO and considerable full-spectrum photoFenton-like catalytic activity. By further increasing the calcination temperature to 400 °C, the hexagonal phase ZnO (JCPDS card no. 36–1451) is observed to appear, while the absorption capacity and photoFenton-like catalytic activity of the calcination product do not change significantly. As the calcination temperature increases to 600 °C, hexagonal phase ZnO and monoclinic phase CuO (JCPDS card no. 45–0937) are found to appear in the calcination product. The MO absorption capacity is significantly reduced while the photoFenton-like catalytic activity is significantly improved especially under irradiation by UV

and NIR light. This observation demonstrates that the occurrence of CuO favors the development of NIR photoFenton-like catalytic activity for the calcination product.

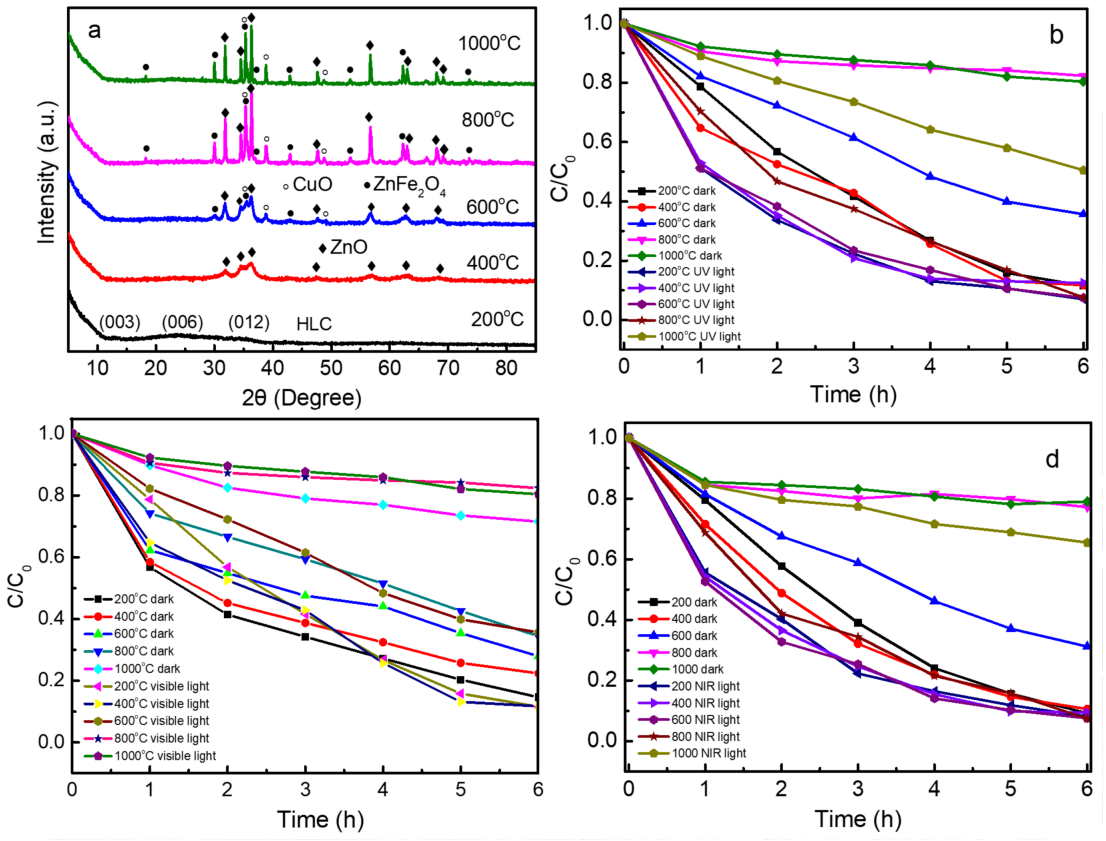

Figure 1. (**a**) X-ray diffraction (XRD) patterns for the ZnO/CuO/$ZnFe_2O_4$ nanocomposite derived from calcination for 3 h at different temperatures; photocatalytic activity for various ZnO/CuO/$ZnFe_2O_4$ nanocomposites in the presence of 1.0 mL of 10 wt. % H_2O_2 under (**b**) UV, (**c**) visible and (**d**) NIR light.

When the calcination temperature reaches 800 °C, the spinel cubic phase $ZnFe_2O_4$ (JCPDS card no. 22–1012) is formed in the calcination product, with ZnO and CuO crystal size significantly increased, judging from the XRD patterns. However, no spinel phase assigned to $CuFe_2O_4$ was found in the corresponding calcination product. Meanwhile, the adsorption capacity of the calcination product is further remarkably reduced while its photoFenton-like catalytic activity is further improved probably due to the formation of $ZnFe_2O_4$. The crystal phases of the calcination product do not change significantly after further increasing the temperature to 1000 °C. Nevertheless, the adsorption capacity of the calcination product is slightly decreased, and its photoFenton-like catalytic activity is greatly lowered, suggesting the importance of adsorption for the photoFenton catalytic degradation of MO. Therefore, for the production of the ZnO/CuO/$ZnFe_2O_4$ nanocomposite, the calcination temperature was chosen to be 800 °C.

2.2. Characterization

The morphology and microstructure of the ZnO/CuO/$ZnFe_2O_4$ nanocomposite derived from calcination at 800 °C were analyzed using field emission scanning electron microscopy (FE-SEM) and high-resolution transmission electron microscopy (HR-TEM), respectively. Figure 2 shows the FE-SEM images of the ZnO/CuO/$ZnFe_2O_4$ nanocomposite and its precursor, as well as the TEM and HR-TEM images of the ZnO/CuO/$ZnFe_2O_4$ nanocomposite. The insets in Figure 2d show the magnified images and Fourier transform electron diffraction (FTED) patterns for the corresponding components.

The FE-SEM images shown in Figure 2a,b reveal that the precursor of the $ZnO/CuO/ZnFe_2O_4$ nanocomposite, i.e., the coprecipitation product of Zn^{2+}, Cu^{2+} and Fe^{3+}, consists of irregular nanoparticles with particle sizes ranging from 10 to 30 nm. The $ZnO/CuO/ZnFe_2O_4$ nanocomposite derived from calcination of the precursor at 800 °C also consists of irregular particles. The particle size falls in the range of 100–200 nm, which is much greater than that the size of the precursor due to the intergrowth of various crystal phases.

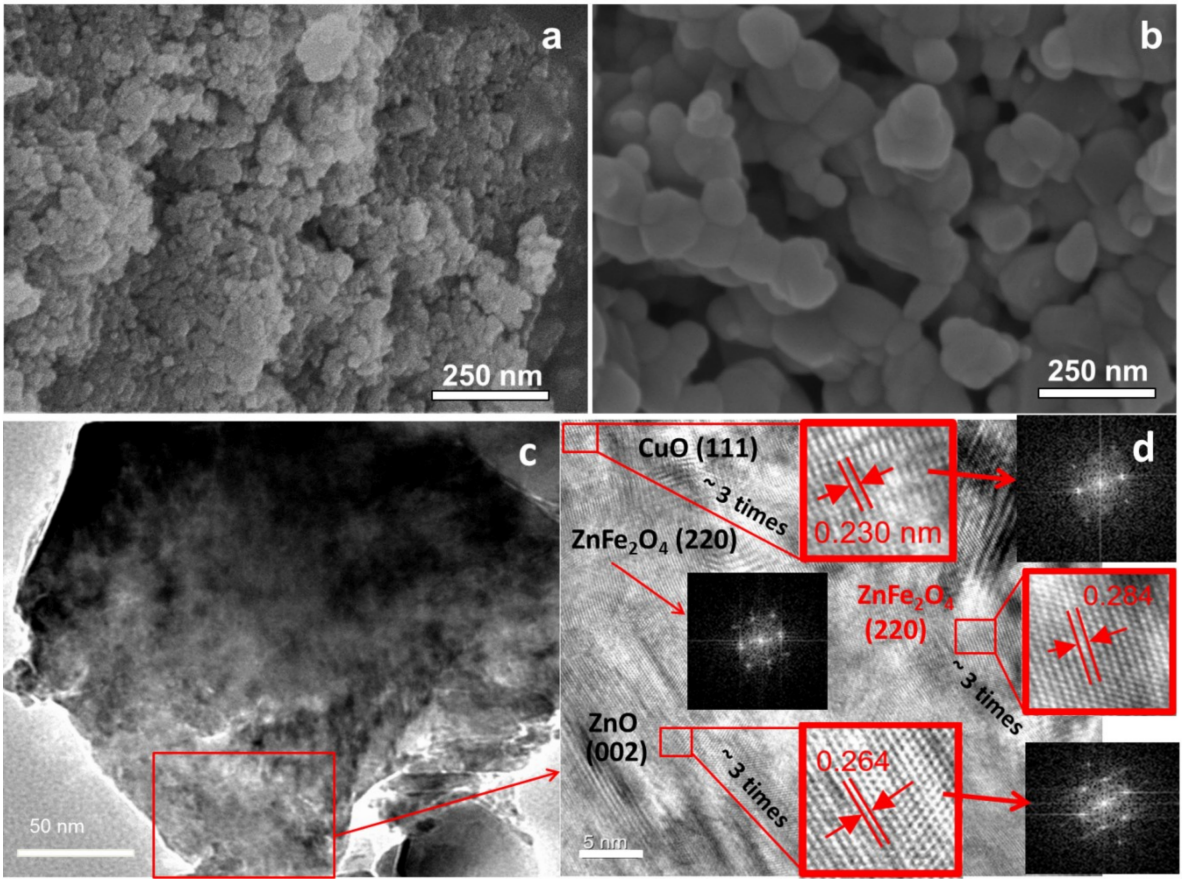

Figure 2. FE-SEM images of (**a**) the precursor of $ZnO/CuO/ZnFe_2O_4$ nanocomposite and (**b**) $ZnO/CuO/ZnFe_2O_4$ nanocomposite; (**c**) TEM and (**d**) HR-TEM images of the $ZnO/CuO/ZnFe_2O_4$ nanocomposite. The insets in (**d**) show the magnified images and Fourier transform electron diffraction (FTED) patterns for the corresponding components.

The TEM and HR-TEM images as well as the FTED patterns shown in Figure 2c,d indicate that the irregular particles in the $ZnO/CuO/ZnFe_2O_4$ nanocomposite are composed of well-crystallized monoclinic CuO, cubic $ZnFe_2O_4$ and hexagonal ZnO, corroborating the results from the XRD analysis. The CuO, ZnO and $ZnFe_2O_4$ crystals grow together. Transitions and distortions of lattice fringes are observed among these crystals, yet no clear interface is formed. This observation indicates that the $ZnO/CuO/ZnFe_2O_4$ nanocomposite is a symbiotic crystal of ZnO, CuO and $ZnFe_2O_4$, which formed the crystal simultaneously from the coprecipitation product of Zn^{2+}, Cu^{2+} and Fe^{3+} without being well-separated.

The chemical states of the $ZnO/CuOZnFe_2O_4$ nanocomposite were analyzed using X-ray photoelectron spectroscopy (XPS). Figure 3 shows the core-level XPS spectra measured for Zn 2p, Cu 2p, Fe 2p and O 1s for the $ZnO/CuOZnFe_2O_4$ nanocomposite. As shown in Figure 3a, the Zn 2p core-level XPS spectrum shows two peaks at binding energies of 1045.0 eV and 1021.9 eV, which are assigned to Zn $2p_{1/2}$ and Zn $2p_{3/2}$ of tetrahedral Zn^{2+}, respectively [29], confirming that the oxidation state of Zn is +2 in the $ZnO/CuOZnFe_2O_4$ nanocomposite.

In the Cu 2p spectrum for the $ZnO/CuOZnFe_2O_4$ nanocomposite, as shown in Figure 3b, two main peaks are observed assigned to Cu $2p_{1/2}$ and Cu $2p_{3/2}$, located at 953.7 eV and 933.8 eV, respectively. In addition, two satellite peaks due Cu $2p_{3/2}$ are found, corroborating the element Cu occurring as CuO in the $ZnO/CuOZnFe_2O_4$ nanocomposite [30]. In the Fe 2p spectrum ranging from 730 to 705 eV (Figure 3c), two main peaks belonging to Fe $2p_{1/2}$ and Fe $2p_{3/2}$ appear at 725.3 eV and 711.6 eV, while the satellite peak of Fe $2p_{3/2}$ is located at 719.3 eV, indicative of the presence of Fe as Fe^{3+} [29,31]. The Fe $2p_{2/3}$ binding energy value of 711.6 eV matches well with that for Fe $2p_{3/2}$ in $ZnFe_2O_4$ [32]. Meanwhile, the Fe $2p_{3/2}$ peak can be deconvoluted into two peaks located at 712.5 eV and 711.2 eV, which are assigned to octahedral and tetrahedral Fe^{3+}, respectively [31]. This observation indicates that the spinel $ZnFe_2O_4$ in the $ZnO/CuOZnFe_2O_4$ nanocomposite has a partially inverse spinel structure [29].

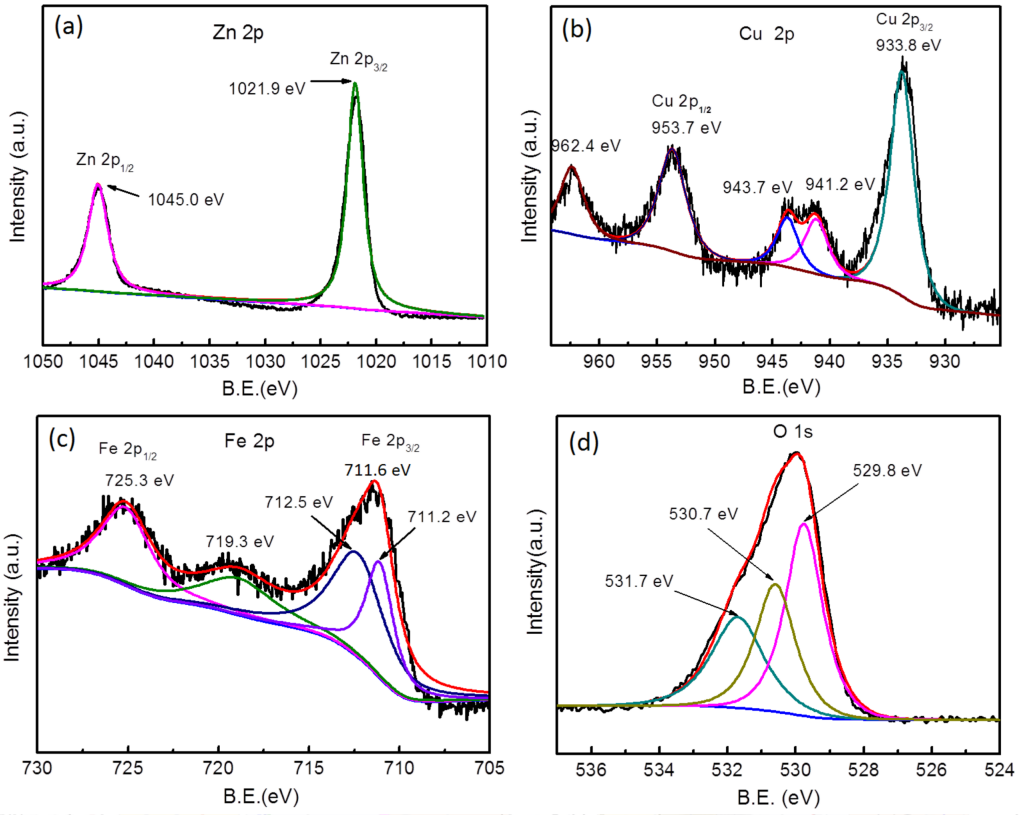

Figure 3. Core-level XPS spectra for (**a**) Zn 2p, (**b**) Cu 2p, (**c**) Fe 2p and (**d**) O 1s for the $ZnO/CuOZnFe_2O_4$ nanocomposite.

The O 1s spectrum shown in Figure 3d displays an asymmetric peak, which can be deconvoluted into three peaks: a low bonding energy peak at 529.8 eV, a middle binding energy peak at 530.7 eV and a high binding energy peak at 531.7 eV. The low binding energy peak is assigned to lattice oxygen O^{2-} from the Zn–O, Cu–O and Fe–O linkages [28,29]. It is much stronger than the other two binding energy peaks, indicating that the majority of oxygen occurs as lattice oxygen O^{2-} in the $ZnO/CuO/ZnFe_2O_4$ nanocomposite [33]. The middle binding energy peak is associated with O^{2-} in the oxygen-deficient regions, indicative of the presence of oxygen vacancies in the $ZnO/CuO/ZnFe_2O_4$ nanocomposite [29]. The high binding energy peak is attributed to the absorbed oxygen species such as O_2, H_2O and CO_2 [33]; this peak is weaker than the other two binding energy peaks due to the high crystallinity of the $ZnO/CuO/ZnFe_2O_4$ nanocomposite.

2.3. Photo-Fenton-like Catalytic Activity

The photoFention-like catalytic activities for the $ZnO/CuO/ZnFe_2O_4$ nanocomposite under UV, visible and NIR light irradiation were further investigated by varying the amount of H_2O_2. To determine if the catalytic degradation of MO in the presence of the $ZnO/CuO/ZnFe_2O_4$ nanocomposite and H_2O_2 is initiated by light, H_2O_2 or their simultaneous action, the removal rates for MO were also analyzed in the presence of the $ZnO/CuO/ZnFe_2O_4$ nanocomposite in the dark, in the presence of the $ZnO/CuO/ZnFe_2O_4$ nanocomposite and H_2O_2 in the dark as well in the presence of the $ZnO/CuO/ZnFe_2O_4$ nanocomposite under light irradiation. The stability of the photoFenton-like catalyst reported in this work, $ZnO/CuO/ZnFe_2O_4$, was evaluated by performing cycle analyses, with the results shown in Figure 4.

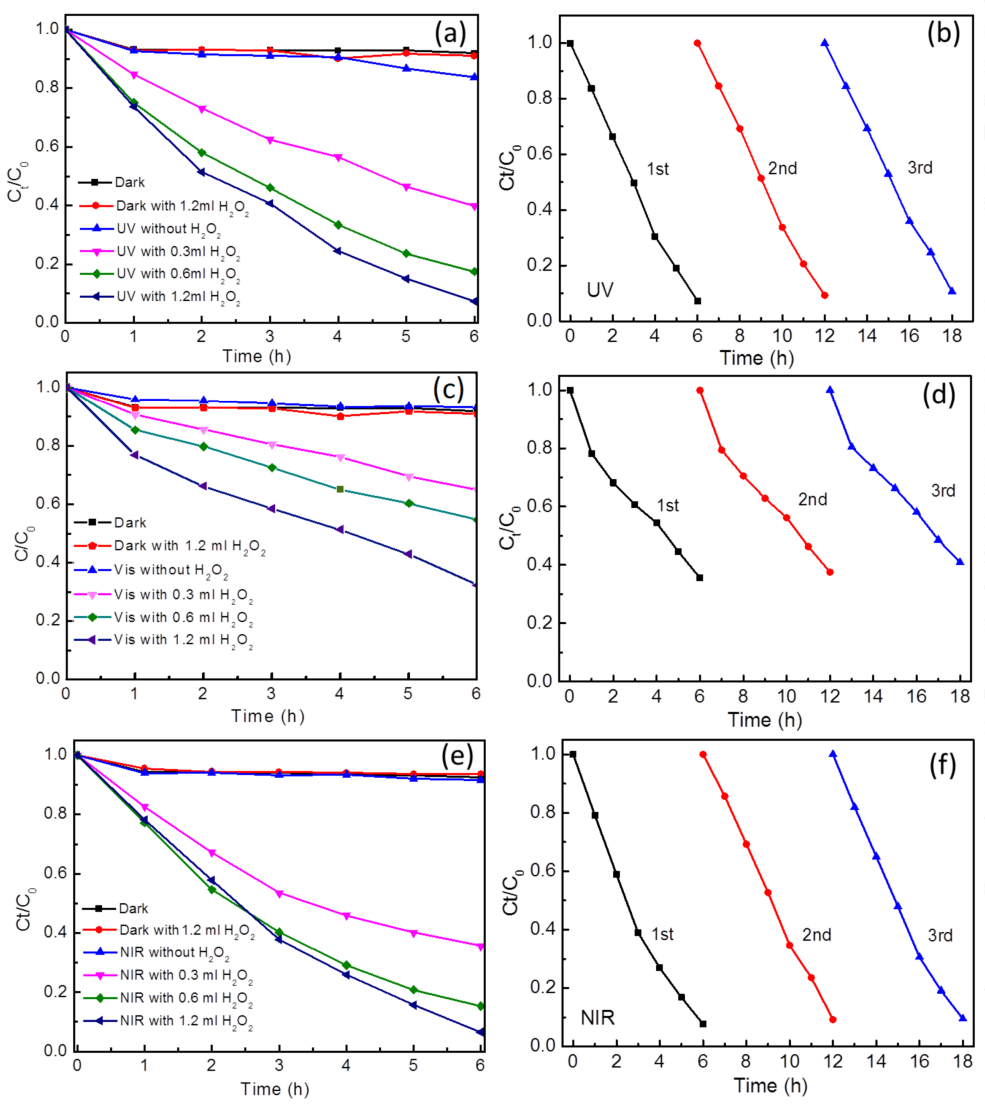

Figure 4. Photocatalytic degradation of MO using $ZnO/CuO/ZnFe_2O_4$ nanocomposite (left) and recycled $ZnO/CuO/ZnFe_2O_4$ nanocomposite (right) in the presence of H_2O_2 under (**a**,**b**) UV, (**c**,**d**) visible and (**e**,**f**) NIR light irradiation. The concentration of H_2O_2 is 10 wt. %. The experiments using recycled $ZnO/ZnFe_2O_4$ nanocomposite were carried out in the presence of 1.2 mL of H_2O_2.

As shown in Figure 4a,c,e, the combination of the $ZnO/CuO/ZnFe_2O_4$ nanocomposite with H_2O_2 (1.2 mL) without light irradiation cannot significantly improve the MO removal rate, compared to the adsorption of the $ZnO/CuO/ZnFe_2O_4$ nanocomposite in the dark, indicating

that the $ZnO/CuO/ZnFe_2O_4$ nanocomposite is not a competent Fenton catalyst. Exposure of the $ZnO/CuO/ZnFe_2O_4$ nanocomposite to UV light only slightly improves the MO removal rate, while exposure to visible or NIR light does not grant any significant improvement for the removal of MO, implying that the $ZnO/CuO/ZnFe_2O_4$ nanocomposite is not a broad-spectrum photocatalyst. However, the introduction of H_2O_2 does not only significantly improve the UV photocatalytic activity of the $ZnO/CuO/ZnFe_2O_4$ nanocomposite but also produces visible and NIR photodegradation effects on MO, confirming the full-spectrum photocatalytic activity of $ZnO/CuO/ZnFe_2O_4$ nanocomposite as a photoFenton-like catalyst. Meanwhile, the photocatalytic activities of the $ZnO/CuO/ZnFe_2O_4$ nanocomposite under UV, visible and NIR light are further improved by increasing the amount of H_2O_2. When the amount of H_2O_2 is increased from 0.3 to 1.2 mL, the MO removal rate can be further increased from 60.1% to 93.1% under UV light irradiation, from 32.3% to 67.8 under visible light irradiation, and from 64.3% to 93.4% under NIR light irradiation, respectively.

As shown in Figure 4b,d,f, the $ZnO/CuO/ZnFe_2O_4$ nanocomposite is very stable under UV, visible and NIR light irradiation as a photoFenton-like catalyst. The MO removal rates are only reduced by 3.6%, 5.3% and 1.8% under UV, visible and NIR light irradiation, respectively, after the $ZnO/CuO/ZnFe_2O_4$ nanocomposite is repeatedly used three times. The slight reduction of the photocatalytic efficiency after repeated use is probably due to contamination and loss of the catalyst during separation.

2.4. Optical Properties and Photocurrent Response

To explain the origin for the full-spectrum photoFenton-like catalytic activity of $ZnO/CuO/ZnFe_2O_4$ nanocomposite, especially in the NIR light region, its optical absorption properties were analyzed using UV-vis-NIR diffuse reflectance spectroscopy, with its transient photocurrent response in the presence of H_2O_2 under NIR light irradiation analyzed using an electrochemical workstation. Figure 5a shows the UV-vis-NIR diffuse reflectance spectrum (DRS) for the $ZnO/CuO/ZnFe_2O_4$ nanocomposite compared to that for ZnO and the $ZnO/ZnFe_2O_4$ nanocomposite. ZnO only shows absorption in the UV region with an absorption edge of 386 nm. The $ZnO/ZnFe_2O_4$ nanocomposite extends the optical absorption to the visible light region with an absorption edge of 788 nm due to the incorporation of $ZnFe_2O_4$. The $ZnO/CuO/ZnFe_2O_4$ nanocomposite further extends the optical absorption to the NIR light region with an absorption edge of 968 nm due to the introduction of CuO. This full-spectrum light absorption for the $ZnO/CuO/ZnFe_2O_4$ nanocomposite provides the prerequisite for the $ZnO/CuO/ZnFe_2O_4$ nanocomposite to produce full-spectrum photoFenton-like catalytic activity.

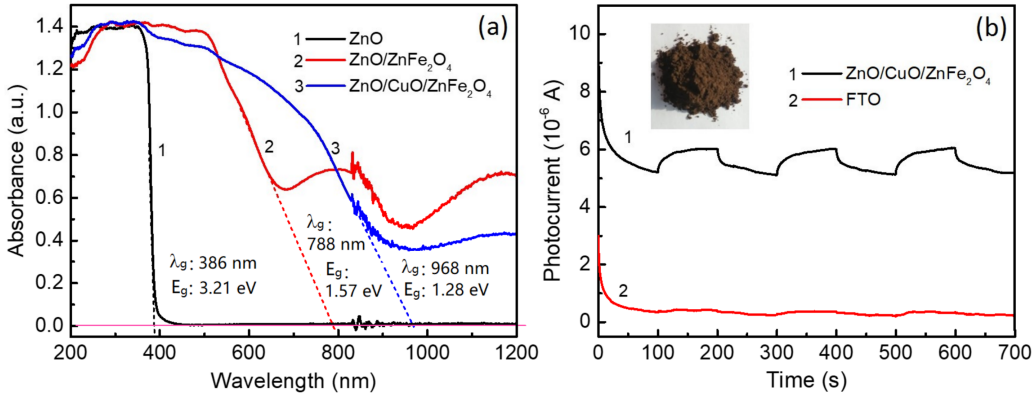

Figure 5. (**a**) UV-vis-NIR diffuse reflectance spectra (DRS) for ZnO, $ZnO/ZnFe_2O_4$ and the $ZnO/CuO/ZnFe_2O_4$ nanocomposite; (**b**) photocurrent generation for the $ZnO/CuO/ZnFe_2O_4$ nanocomposite in the presence of H_2O_2 under NIR light. The inset in plane b shows a photograph of the $ZnO/CuO/ZnFe_2O_4$ nanocomposite.

From the equation $E_g = 1240/\lambda_g$ and the absorption edges (λ_g) acquired from DRS, the band gaps (E_g) for ZnO, ZnO/$ZnFe_2O_4$, and the ZnO/CuO/$ZnFe_2O_4$ nanocomposite can be estimated to be 3.21 eV, 1.57 eV and 1.28 eV, respectively. The E_g values for ZnO/$ZnFe_2O_4$ and the ZnO/CuO/$ZnFe_2O_4$ nanocomposite are very similar to that of $ZnFe_2O_4$ [29] and CuO [28]. Therefore, the energy bands for CuO and $ZnFe_2O_4$ in the ZnO/CuO/$ZnFe_2O_4$ nanocomposite must determine the same in the ZnO/CuO/$ZnFe_2O_4$ nanocomposite. The two bands can be estimated to be 1.57 eV and 1.28 eV using the absorption edge for ZnO/CuO/$ZnFe_2O_4$ and the ZnO/$ZnFe_2O_4$ nanocomposite, respectively.

In a photoFenton-like process, H_2O_2 acts as an electron acceptor for reacting with the photogenerated electrons, providing hydroxyl radicals (•OH) for the degradation of organic pollutant [29,34]. To produce •OH in the presence of H_2O_2, the photogenerated electrons in the ZnO/CuO/$ZnFe_2O_4$ nanocomposite should have a potential lower than the redox potential of H_2O_2/•OH (+0.38 eV), i.e., the conduction band (CB) potential of either ZnO, CuO or $ZnFe_2O_4$ should be lower than +0.38 eV. The CB potentials for ZnO, $ZnFe_2O_4$ and CuO were calculated to be −0.32 eV, +0.58 eV and +0.67 eV, respectively, according to their band gap energies and the concept of Mulliken's electronegativity [28]. The ZnO/CuO/$ZnFe_2O_4$ nanocomposite cannot provide •OH in the presence of H_2O_2 under visible light or NIR light irradiation if the ZnO, $ZnFe_2O_4$ and CuO components occur as a physical mixture, since neither $ZnFe_2O_4$ nor CuO can generate electrons acceptable to H_2O_2.

Figure 5b shows the transient photocurrent response of the ZnO/CuO/$ZnFe_2O_4$ nanocomposite under NIR light irradiation in the presence of H_2O_2 with on–off switch times of 100 s. As shown in Figure 5b, the ZnO/CuO/$ZnFe_2O_4$ nanocomposite produces a strong transient photocurrent in the presence of H_2O_2 under NIR irradiation, while the fluorine-doped tin oxide (FTO) glass hardly shows any photocurrent response under the same conditions. This observation implies that the ZnO/CuO/$ZnFe_2O_4$ nanocomposite possesses high transfer efficiency for photogenerated electrons and good separation of photogenerated electron–hole pairs in the presence of H_2O_2 under NIR light irradiation [17,29].

2.5. Suggested Photocatalytic Mechanism

Based on the above investigations, the excitation and transfer processes for the charge carriers under light irradiation, as well as the production of •OH, which are the active species in the photoFenton-like process, are shown in Figure 6.

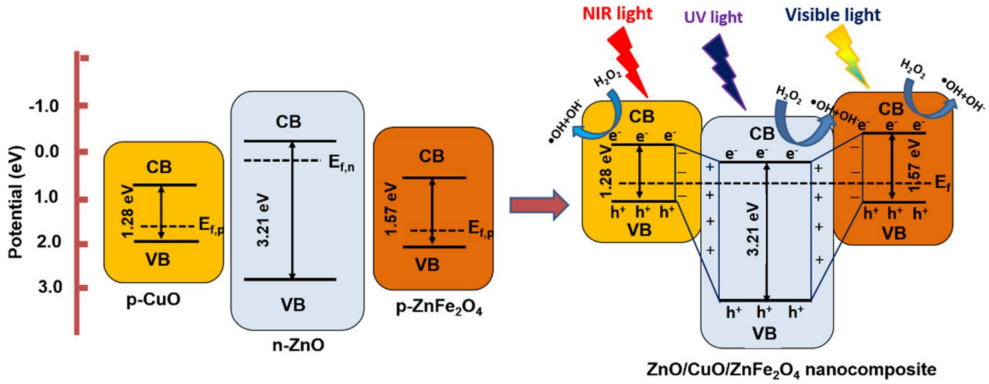

Figure 6. Schematic diagram for p-n-p heterojunction formation in the ZnO/CuO/$ZnFe_2O_4$ nanocomposite and the excitation and transfer process for charge carriers in the ZnO/CuO/$ZnFe_2O_4$ nanocomposite under light irradiation.

The formation of p-n-p heterojunctions shown in Figure 6 is reasonably expected, as is evident from the transitions and distortions of the lattice fringes observed among the n-ZnO, p-CuO and p-$ZnFe_2O_4$ nanocrystals (Figure 2d), and the diffusion of electrons (e^-) from n-ZnO to p-CuO and p-$ZnFe_2O_4$ as well as holes (h^+) from p-CuO and p-$ZnFe_2O_4$ to n-ZnO in the ZnO/CuO/$ZnFe_2O_4$

nanocomposite. The formation of the p-n-p junction causes the energy bands in n-ZnO to bend downwards and enables the energy bands in p-CuO and p-$ZnFe_2O_4$ to bend upwards to form a unified Fermi level among the ZnO, CuO and $ZnFe_2O_4$ nanocrystals. Consequently, the CB potentials for CuO and $ZnFe_2O_4$ become even lower than that for ZnO. The photogenerated electrons in the CuO and $ZnFe_2O_4$ components under visible and NIR light irradiation can, therefore, either be captured by H_2O_2 to form •OH, which can oxidize organic pollutants such as MO, or transfer to the CB of the ZnO component, leading to the separation of photogenerated electrons and holes.

3. Experimental

3.1. Preparation of the ZnO/CuO/$ZnFe_2O_4$ Nanocomposite

The precursor for the ZnO/CuO/$ZnFe_2O_4$ nanocomposite was synthesized using a coprecipitation method [35]. A mixed salt aqueous solution containing 0.045 M $Zn(NO_3)_2{\cdot}6H_2O$, 0.015 M $Cu(NO_3)_2{\cdot}3H_2O$ and 0.02 M $Fe(NO_3)_3{\cdot}9H_2O$ and a mixed alkali aqueous solution containing 0.35 M NaOH and 0.05 M Na_2CO_3 were simultaneously added dropwise to vigorously stirred distilled water at a rate where the pH remained at approximately 10.5. After this addition, the resulting slurry was mixed for 30 min and aged at 65 °C for 3 h. This slurry was then filtered, thoroughly washed with deionized water, dried at 50 °C for 24 h, and milled to obtain the precursor. The precursor was heated to 800 °C in an electric tubular furnace at a rate of 2 °C min^{-1} before being calcined for 3 h. After being cooled naturally to room temperature, the product was milled to obtain the ZnO/CuO/$ZnFe_2O_4$ nanocomposite.

ZnO nanoparticles and the ZnO/$ZnFe_2O_4$ nanocomposite were also prepared using similar coprecipitation and calcination procedures, except that the $Cu(NO_3)_2{\cdot}3H_2O$ and $Fe(NO_3)_3{\cdot}9H_2O$ were replaced by the same mole of $Zn(NO_3)_2{\cdot}6H_2O$, and $Cu(NO_3)_2{\cdot}3H_2O$ was replaced by the same mole of $Zn(NO_3)_2{\cdot}6H_2O$.

3.2. Characterization

The XRD patterns for the various calcination products were recorded using a Bruke D8 Advance powder X-ray diffractometer (Karlsruhe, Germany) with Cu Kα radiation (λ = 0.15406 nm). The FE-SEM and HR-TEM images of the samples were obtained with a Hitachi S-4800 field emission scanning electron microscope (Hitachi, Tokyo, Japan) and a JOEL JEM-2100 high-resolution transmission electron microscope (Akishima, Tokyo, Japan), respectively. The XPS spectra were collected by an ESCALAB 250 spectrometer (VG Scientific Ltd., United Kingdom) equipped with a monochromatized Al Kα X-ray source. All of the binding energies were calibrated C1s peak at a binding energy of 284.6 eV. The UV–Vis-NIR DRS were recorded on a spectrophotometer (Cary 5000, Varian, Inc., Palo Alto, CA, USA) with an integrating sphere attachment in the wavelength range of 200–1200 nm. The transient photocurrents were measured using a CHI660E electrochemical workstation (Chenhua Ins. Inc., Shanghai, China) with a standard three-electrode assembly, where Ag/AgCl was used as the reference electrode, a Pt wire was used as the counter electrode, and ZnO/CuO/$ZnFe_2O_4$ nanocomposite-coated FTO conductive glass (Zhuhai Kaivo Optoelectronic Technology Co., Ltd., Zhuhai, China) was used as the working electrode. The electrolyte was a 0.5 M Na_2SO_4 aqueous solution [29].

3.3. Photocatalytic Activity Test

Photocatalytic experiments under UV and visible light irradiation were carried out in a photocatalytic reactor at 25 °C. A 500 W mercury lamp with a primary wavelength of 365 nm and a 350 W Xe arc lamp equipped with an UV optical filter with a cutoff wavelength of 380 nm were used as UV light and visible light sources, respectively. Experiments under NIR light irradiation were performed at a temperature below 30 °C in a self-assembled experimental device, as reported previously [17,29]. A 200 W infrared lamp with a cutoff filter for cutting off the light below 800 nm was

employed as the near-infrared source. 20 mg of the nanocomposite sample was suspended in 20 mL of 20 mg/L MO aqueous solution followed by sonication for several seconds; then, a predetermined amount of H_2O_2 (10 wt. %) was added. The above suspension either remained in the dark or was irradiated under UV, visible or NIR light. At given time intervals, 3 mL of suspension was collected and immediately centrifuged to remove the solid catalyst at 10000 rpm for 5 min. The residual concentration of MO solution was determined by measuring its absorbance at 465 nm with a UV-Vis spectrophotometer (Hitachi UV-300, Tokyo, Japan).

4. Conclusions

By calcinating the coprecipitation product of Zn^{2+}, Cu^{2+} and Fe^{3+} at different temperatures, a series of nanocomposites with UV, visible and NIR photocatalytic activities in the presence of H_2O_2 were prepared. Among the various nanocomposites, the ZnO/CuO/$ZnFe_2O_4$ nanocomposite derived from calcination at 800 °C composed of ZnO, CuO and $ZnFe_2O_4$ nanocrystal heterojunctions shows the highest photoFenton-like activity. The $ZnFe_2O_4$ and CuO components extend the optical absorption of the ZnO/CuO/$ZnFe_2O_4$ nanocomposite to the visible and NIR regions, respectively. The presence of H_2O_2 promotes the separation of photogenerated electrons and holes and confers the ZnO/CuO/$ZnFe_2O_4$ nanocomposite with full-spectrum photocatalytic activity. The photocatalytic activity of the ZnO/CuO/$ZnFe_2O_4$ nanocomposite is improved by increasing the amount of H_2O_2 and remains mostly unchanged after undergoing three cycles of repeated use. The ZnO/CuO/$ZnFe_2O_4$ nanocomposite is a promising full-spectrum photoFenton-like catalyst for the degradation of organic pollutants.

Author Contributions: Conceptualization, W.L.; Investigation, Z.L. and H.C; Funding acquisition, W.L.; Validation: Z.L, H.C. and W.L.

Acknowledgments: The project was funded by the National Natural Science Foundation of China (Grant No. 31270625).

Conflicts of Interest: The authors declare no conflict of interest.

References

1. Wang, Q.; O'Hare, D. Recent advances in the synthesis and application of layered double hydroxide (LDH) nanosheets. *Chem. Rev.* **2012**, *112*, 4124–4155. [CrossRef] [PubMed]
2. Meng, Y.; Luo, W.; Xia, S.; Ni, Z. Preparation of Salen–metal complexes (metal = Co or Ni) intercalated ZnCr-LDHs and their photocatalytic degradation of Rhodamine B. *Catalysts* **2017**, *7*, 143. [CrossRef]
3. Prevot, V.; Tokudome, Y. 3D hierarchical and porous layered double hydroxide structures: An overview of synthesis methods and applications. *J. Mater. Sci.* **2017**, *52*, 11229–11250. [CrossRef]
4. Carja, G.; Grosu, E.F.; Mureseanu, M.; Lutic, D. A family of solar light responsive photocatalysts obtained using Zn^{2+} Me^{3+} (Me = Al/Ga) LDHs doped with Ga_2O_3 and In_2O_3 and their derived mixed oxides: A case study of phenol/4-nitrophenol decomposition. *Catal. Sci. Technol.* **2017**, *7*, 5402–5412. [CrossRef]
5. Wang, J.; Zhang, T.; Li, K.; Cao, Y.; Zeng, Y. Dehydrogenation catalysts for synthesis of O-phenylphenol via Cu/Ni/Mg/Al hydrotalcite-like compounds as precursors. *Catalysts* **2018**, *8*, 186. [CrossRef]
6. Chowdhury, P.R.; Bhattacharyya, K.G. Ni/Ti layered double hydroxide: Synthesis, characterization and application as a photocatalyst for visible light degradation of aqueous methylene blue. *Dalton Trans.* **2015**, *44*, 6809–6824. [CrossRef] [PubMed]
7. Xiang, X.; Xie, L.; Li, Z.; Li, F. Ternary MgO/ZnO/In_2O_3 heterostructured photocatalysts derived from a layered precursor and visible-light-induced hotocatalytic activity. *Chem. Eng. J.* **2013**, *221*, 222–229. [CrossRef]
8. Huo, R.; Kuang, Y.; Zhao, Z.; Zhang, F.; Xu, S. Enhanced photocatalytic performances of hierarchical ZnO/$ZnAl_2O_4$ microsphere derived from layered double hydroxide precursor spray-dried microsphere. *J. Colloid Interface Sci.* **2013**, *407*, 17–21. [CrossRef] [PubMed]

9. Mikami, G.; Grosu, F.; Kawamura, S.; Yoshida, Y.; Carja, G.; Izumi, Y. Harnessing self-supported Au nanoparticles on layered double hydroxides comprising Zn and Al for enhanced phenol decomposition under solar light. *Appl. Catal. B* **2016**, *199*, 260–271. [CrossRef]
10. Nayak, S.; Pradhan, A.C.; Parida, K.M. Topotactic Transformation of solvated MgCr-LDH nanosheets to highly efficient porous $MgO/MgCr_2O_4$ nanocomposite for photocatalytic H_2 evolution. *Inorg. Chem.* **2018**, *57*, 8646–8661. [CrossRef] [PubMed]
11. Kim, S.; Durand, P.; André, E.; Carteret, C. Enhanced photocatalytic ability of Cu, Co doped ZnAl based mixed metal oxides derived from layered double hydroxides. *Colloids Surf. A* **2017**, *524*, 43–52. [CrossRef]
12. Pan, D.; Ge, S.; Zhao, J.; Shao, Q.; Guo, L.; Zhang, X.; Lin, J.; Xu, G.; Guo, Z. Synthesis, characterization and photocatalytic activity of mixed-metal oxides derived from NiCoFe ternary layered double hydroxides. *Dalton Trans.* **2018**, *47*, 9765–9778. [CrossRef] [PubMed]
13. Yang, Q.; Wang, S.; Chen, F.; Luo, K.; Sun, J.; Gong, C.; Yao, F.; Wang, X.; Wu, J.; Li, X.; et al. Enhanced visible-light-driven photocatalytic removal of refractory pollutants by Zn/Fe mixed metal oxide derived from layered double hydroxide. *Catal. Commun.* **2017**, *99*, 15–19. [CrossRef]
14. Chen, M.; Wu, P.; Wei, Q.; Zhu, Y.; Yang, S.; Ju, L.; Zhu, N.; Lin, Z. The role of oxygen vacancy over ZnCr-layered double oxide in enhancing solar light-driven photocatalytic degradation of bisphenol. A. *Environ. Chem.* **2018**, *15*, 226–235. [CrossRef]
15. Zhang, G.; Hu, L.; Zhao, R.; Su, R.; Wang, Q.; Wang, P. Microwave-assisted synthesis of ZnNiAl-layered double hydroxides with calcination treatment for enhanced PNP photo-degradation under visible-light irradiation. *J. Photochem. Photobiol. A* **2018**, *356*, 633–641. [CrossRef]
16. Goswami, K.; Ananthakrishnan, R.; Mandal, S. Facile synthesis of cation doped $ZnO\text{-}ZnCo_2O_4$ hetero-nanocomposites for photocatalytic decomposition of aqueous organics under visible light. *Mater. Chem. Phys.* **2018**, *206*, 174–185. [CrossRef]
17. Gao, W.; Liu, W.; Leng, Y.; Wang, X.; Wang, X.; Hu, B.; Yu, D.; Sang, Y.; Liu, H. In2S3 nanomaterial as a broadband spectrum photocatalyst to display significant activity. *Appl. Catal. B* **2015**, *176*, 83–90. [CrossRef]
18. Zhou, Y.; Liu, P.; Jiang, F.; Tian, J.; Cui, H.; Yang, J. Vanadium sulfide sub-microspheres: A new near-infrared-driven photocatalyst. *J. Colloid Interface Sci.* **2017**, *498*, 442–448. [CrossRef] [PubMed]
19. Feng, R.; Lei, W.; Sui, X.; Liu, X.; Qi, X.; Tang, K.; Liu, G.; Liu, M. Anchoring black phosphorus quantum dots on molybdenum disulfide nanosheets: A 0D/2D nanohybrid with enhanced visible−and NIR −light photoactivity. *Appl. Catal. B* **2018**, *238*, 444–453. [CrossRef]
20. Wang, X.; Wang, F.; Sang, Y.; Liu, H. Full-spectrum solar-light-activated photocatalysts for light–chemical energy conversion. *Adv. Energy Mater.* **2017**, *7*, 1700473. [CrossRef]
21. Chen, J.; Liu, W.; Li, Z.; Liu, H. Thermally-assisted photodegradation of lignin by TiO_2/H_2O_2 under visible/near-infrared light irradiation. *Sci. China. Mater.* **2018**, *61*, 382–390. [CrossRef]
22. Yang, M.-Q.; Gao, M.; Hong, M.; Ho, G.W. Visible-to-NIR photon harvesting: Progressive engineering of catalysts for solar-powered environmental purification and fuel production. *Adv. Mater.* **2018**, 1802894. [CrossRef] [PubMed]
23. Acosta-Mora, P.; Domen, K.; Hisatomi, T.; Lyu, H.; Méndez-Ramos, J.; Ruiz-Morales, J.C.; Khaidukov, N.M. Shifting the NIR into the UV-blue: Up-conversion boosted photocatalysis. *Opt. Mater.* **2018**, *83*, 315–320. [CrossRef]
24. Li, L.; Zhang, M.; Zhao, Z.; Sun, B.; Zhang, X. Visible/near-IR-light-driven TNFePc/BiOCl organic–inorganic heterostructures with enhanced photocatalytic activity. *Dalton Trans.* **2016**, *45*, 9497–9505. [CrossRef] [PubMed]
25. Chen, J.; Liu, W.; Gao, W. Tuning photocatalytic activity of In_2S_3 broadband spectrum photocatalyst based on morphology. *Appl. Surf. Sci.* **2016**, *368*, 288–297. [CrossRef]
26. Tian, J.; Sang, Y.; Yu, G.; Jiang, H.; Mu, X.; Liu, H. A Bi_2WO_6-based hybrid photocatalyst with broad spectrum photocatalytic properties under UV, visible, and near-infrared irradiation. *Adv. Mater.* **2013**, *25*, 5075–5080. [CrossRef] [PubMed]
27. Qin, Z.; Liu, W.; Li, Z.; Chen, H.; Li, G.; Yu, D. Er^{3+}-doped $ZnO/ZnAl_2O_4$ multi-phase oxides acting as near-infrared active photocatalyst. *J. Mater. Sci. - Mater. Electron.* **2018**, *29*, 8293–8302. [CrossRef]
28. Chen, H.; Liu, W.; Hu, B.; Qin, Z.; Liu, H. A full-spectrum photocatalyst with strong near-infrared photoactivity derived from synergy of nano-heterostructured Er^{3+}-doped multi-phase oxides. *Nanoscale* **2017**, *9*, 18940–18950. [CrossRef] [PubMed]

29. Chen, H.; Liu, W.; Qin, Z. ZnO/$ZnFe_2O_4$ nanocomposite as a broadspectrum photo-Fenton-like photocatalyst with near-infrared activity. *Catal. Sci. Technol.* **2017**, *7*, 2236–2244. [CrossRef]
30. Tougaard, S.M. Determination of the Cu 2p primary excitation spectra for Cu, Cu_2O and CuO. *Surf. Sci.* **2014**, *620*, 17–22. [CrossRef]
31. Grosvenor, A.P.; Kobe, B.A.; Biesinger, M.C.; McIntyre, N.S. Investigation of multiplet splitting of Fe 2p XPS spectra and bonding in iron compounds. *Surf. Interface Anal.* **2004**, *36*, 1564–1574. [CrossRef]
32. Pan, F.; Guo, Y.; Cheng, F.; Fa, T.; Yao, S. Synthesis of $ZnFe_2O_4$ nanomagnets by Fe-ion implantation into ZnO and post-annealing. *Chin. Phys. B* **2011**, *20*, 127501. [CrossRef]
33. Chen, Y.; Xu, X.L.; Zhang, G.H.; Xue, H.; Ma, S.Y. Blue shift of optical band gap in Er-doped ZnO thin films deposited by direct current reactive magnetron sputtering technique. *Physica E* **2010**, *42*, 1713–1716. [CrossRef]
34. Bokare, A.D.; Choi, W. Review of iron-free Fenton-like systems for activating H_2O_2 in advanced oxidation processes. *J. Hazard. Mater.* **2014**, *275*, 121–135. [CrossRef] [PubMed]
35. Hu, B.; Liu, W.; Gao, W.; Han, J.; Liu, H.; Lucia, L.A. Pseudo-Janus Zn/Al-based nanocomposites for Cr(VI) sorption/remediation and evolved photocatalytic functionality. *Chem. Eng. J.* **2015**, *277*, 150–158. [CrossRef]